Metals & corrosion

A comparison of adiabatic shear bands in wrought and additively manufactured 316L stainless steel using nanoindentation and electron backscatter diffraction

Jordan S. Weaver[1,4,*] (iD), Veronica Livescu[2] (iD), and Nathan A. Mara[1,3] (iD)

[1] *Center for Integrated Nanotechnologies, Materials Physics and Applications Division, Los Alamos National Laboratory, P.O. Box 1663, Los Alamos, NM 87545, USA*

[2] *MST-8: Materials Science in Radiation and Dynamic Extremes, Los Alamos National Laboratory, P.O. Box 1663, Los Alamos, NM 87545, USA*

[3] *Department of Chemical Engineering and Materials Science, University of Minnesota-Twin Cities, 421 Washington Ave. SE, Minneapolis, MN 55455, USA*

[4] *Present address: Engineering Laboratory, National Institute of Standards and Technology, 101 Bureau Dr., Gaithersburg, MD 20899, USA*

ABSTRACT

The resistance of stainless steels to shear localization is dependent on processing and microstructure. The amount of research evaluating the shear response of additively manufactured (AM) stainless steels compared to traditionally manufactured ones is limited. To address this gap, experiments were performed on directed energy deposition AM as-built and wrought 316L stainless steel using a forced shear technique with a hat-shaped specimen and a Split-Hopkinson pressure bar. The resulting adiabatic shear bands were characterized with electron backscatter diffraction (EBSD) and nanoindentation to quantify the changes in microstructure and deformation hardening across shear band regions and between the wrought and AM materials. Despite significant differences between the wrought and AM materials including the forced shear response, the postmortem states of work hardening due to the shear band deformation are nearly the same. The maximum nanoindentation stresses occurred in the shear band center with similar magnitudes and only minor differences away from the shear band. Although EBSD data cannot be resolved in the shear band center, misorientation trends, particularly grain reference orientation deviation, were found to closely resemble nanoindentation trends. The combination of EBSD misorientation and nanoindentation, which are linked through changes in dislocation density, is a viable protocol to quantify local changes to macroscopically applied deformation.

Address correspondence to E-mail: jordan.weaver@nist.gov

Introduction

Additive manufacturing (AM) is a maturing technology capable of producing complex parts for a variety of applications; however, generating basic process–structure–property–performance relationships is an ongoing endeavor [1–3]. Here, we focus on directed energy deposition AM 316L stainless steel (316L SS) and its dynamic mechanical behavior. Understanding the dynamic mechanical performance of AM materials is critical for their adoption for crashworthiness and defense applications.

At high strain rates, adiabatic shear localization can occur and lead to failure through unstable deformation. In ductile materials, the formation of adiabatic shear bands is driven by a competition of thermal softening and work hardening [4]. Forced shear testing has been used to study adiabatic shear localization in a variety of materials [5]. In particular, Xue and Gray [4, 6, 7] have completed detailed studies of the evolution of adiabatic shear bands in wrought and cold-rolled 316L SS with interrupted forced shear tests and transmission electron microscopy (TEM). Some of their findings for 316L stainless steel were: the accumulation of a high defect density is a prerequisite for shear band formation, the defects that occur consist largely of dislocations and deformation twins, the local temperature buildup prior to shear is relatively low, pre-straining leads to earlier shear band deformation, and the hardness increases significantly inside the shear band [4, 6, 7]. Quantifying the location specific deformation across the shear band is necessary for understanding the shear localization process.

Quantifying differences in location specific deformation inside a single sample or between different samples due to macroscopically applied deformation can be achieved with electron backscatter diffraction (EBSD) and nanoindentation. Increases in EBSD misorientation measurements in deformed materials represent the accumulation of plastic strain, residual stresses, and/or dislocations [8–13]. Similarly, increases in hardness in deformed samples are often due to the accumulation of plastic strain and increases in dislocations. EBSD was used in recent work on compact force shear band samples of Al and Ti to quantify differences in geometrically necessary dislocation densities in shear band regions [12, 14]. One limitation of this technique is that there is very little information in the shear band center due to pattern degradation caused by severe plastic deformation and/or unresolvable microstructure features (e.g., [12, 14]). In this case, nanoindentation can be used to measure changes in the local flow stress (e.g., [15–19]). Despite the regular use of EBSD and nanoindentation to quantify changes in local deformation due to macroscopically applied deformation, there are very few studies that have quantitatively compared the information from both techniques in such experiments [18–20].

In this study, dynamic forced shear tests using hat-shaped geometry and a Split-Hopkinson pressure bar were used to produce shear bands in annealed wrought and as-built AM 316L SS. These are referred to simply as wrought and AM materials. Deformed samples were characterized using EBSD, nanohardness, and spherical nanoindentation (SNI) stress–strain measurements to quantify the structure and deformation-hardened material across shear band regions. "Materials and methods" section describes the sample pedigree, experiments, and characterization. The EBSD and nanoindentation results are presented in "Results" section. In "Discussion" section, comparisons are made between the wrought and AM materials along with a critical comparison of EBSD misorientation and indentation measurements. This is followed by the main conclusions pertaining to shear bands and their characterization via methods relying on diffraction and/or mechanical contrast in "Conclusions" section.

Materials and methods

Sample pedigree

Samples of wrought and AM 316L SS were used in this study. The annealed wrought material was in the form of 12.5-mm-thick plate [21]. The as-built AM material is described in Ref. [21]. Briefly, it was produced by directed energy deposition additive manufacturing using a LENS MR-7 system from Optomec (Albuquerque, NM) equipped with a 1070-nm Yb-fiber laser. A laser power of 380 W, layer thickness of 0.3 mm, hatch spacing of 0.46 mm, travel speed of 1.12 cm s^{-1}, 90° rotation scan strategy, and powder feed rate of 6.26 g min^{-1} were used to build right-regular, solid cylinders 2.5 cm in diameter and 3.3 cm tall under an argon cover gas. A laser focal

length of 160.4 mm and a focus condition with the focal point $\sim$ 3.8 mm below the surface were used. Gas-atomized powder was sourced from Carpenter Powder Products (Bridgewater, PA) [21, 22]. The annealed wrought plate had an average grain size and texture of 29 μm and 2.0 multiples of random (MRD), respectively, while the as-built AM cylinders had an average grain size and texture of 4.5 μm and 2.7 MRD, respectively [21, 23]. The AM microstructure also contains more complex features compared to the wrought microstructure with a macroscopic fish-scale structure from the melting and re-solidification boundaries, a fine dendritic structure inside grains, and a fine dispersion of submicron particles [21, 23]. Quasi-static and dynamic compression tests show that as-built, AM material has a $\sim$ 60% higher yield strength compared to the annealed wrought plate [21]. Lastly, there are some chemical differences between the powder feedstock and the wrought plate given in Table 1, namely a higher Cr content in the powder. Yadollahi et al. [24] report a chemical composition of AM 316L made using an almost identical process that matches the powder in Table 1. Similarly, Wang et al. [25] showed that the chemical composition remains nearly the same between the powder feedstock and the final part for 304L stainless steel manufactured using the same AM process. Therefore, the reported chemical composition of the powder feedstock is a good approximation of the chemical composition of the final part.

Dynamic forced shear testing

Top-hat samples were machined from the annealed wrought plate and the as-built AM right cylinders. The top-hat specimen dimensions are shown in Fig. 1a. When the specimen is loading axially, shear localization occurs in the regions marked in red. The slight overlap between the top-hat and cylindrical brim creates a mixed loading state combining shear and compressive stress [26–28]. The compressive stress helps restrain mode I cracking in the shear band. However, the slight overlap does not allow for a calculation of the shear strain. The stress–

displacement curves are an alternative measure. AM top-hat specimens were deformed to a maximum displacement of 0.5 mm at a strain rates of approximately 1500 s^{-1}, 2500 s^{-1}, and 3500 s^{-1} using a Split-Hopkinson pressure bar. The bar diameters were 0.5 inches made of grade 350 maraging steel. The striker bar length and pressure varied with a 254 mm bar at 6 psi, 152.4 mm bar at 6 psi, and 88.95 mm bar at 7 psi for the approximate strain rates of 1500 s^{-1}, 2500 s^{-1}, and 3500 s^{-1}, respectively. Deformation was arrested by using tool steel collars placed around specimens. The loading axis is parallel to the build direction. The true shear stress versus displacement curves for the AM material are shown in Fig. 1b. A single wrought specimen was deformed at a strain rate of 2500 s^{-1}. The AM material shows a higher peak stress than the wrought material which continues up to a displacement of 0.2 mm at which the shear stress starts to drop and finishes below the wrought material. An increase in shear stress following a drop in shear stress is also seen in cold-worked 316L SS [7].

Post-deformation characterization

Dynamically forced shear samples were cross-sectioned in half as shown in Fig. 1. Cross-sectioned samples were metallographically ground and polished with a final vibratory polish using 0.06 μm colloidal silica suspension for 12–24 h. EBSD was collected with a FEI XL30 scanning electron microscope (SEM) and TSL EDAX Digiview camera using a step size of 0.6 μm. EBSD data were post-processed in MTEX (v5.0) [29]. The post-process included multiple steps. First, points with very low confidence index (< 0.03) were ignored but not cleaned up or added to existing grains. This leaves a strip of unusable data where the shear band occurs. Second, grains were identified using a misorientation threshold of 5°. The useable data were further reduced by using a minimum grain size (grain size > 9 points). Misorientation calculations were made on this reduced data. Two different misorientation calculations were used: kernel average misorientation (KAM) and grain

Table 1 Chemical composition of powder feedstock and wrought material from the manufacturer reported in Ref. [21]

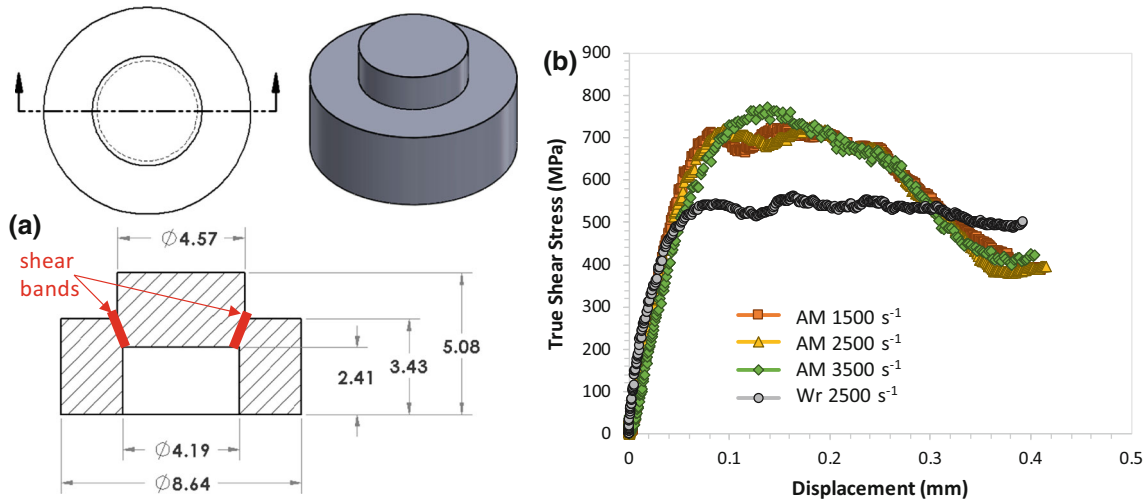| Wt%	C	Cr	Cu	Mn	Mo	N	Ni	P	S	Si
Wrought	0.022	16.16	0.39	1.70	2.08	0.063	10.03	0.029	0.0004	0.40
Powder	0.020	20.70	0.19	1.32	2.45	0.090	11.40	0.020	0.0100	0.50

Figure 1 **a** drawing of hat-shaped sample with a cross-sectional view. Regions marked in red on the cross-sectional view are where shear localization occurs. Dimensions are in millimeters. **b** true shear stress versus displacement curves for additively manufactured (AM) material at three different nominal strain rates and wrought (Wr) material at a single nominal strain rate.

reference orientation deviation (GROD) [8]. The main difference is that KAM uses a local neighborhood called a kernel, whereas GROD uses entire grains for determining the misorientation at each point [8]. KAM was calculated from EBSD data ignoring grain boundaries using the first nearest neighbor and a misorientation threshold of 5°. GROD was also calculated for grains defined by a minimum misorientation of 5° and grain size greater than 9 points. EBSD image quality (IQ) maps were used to determine the shear band center and location of indents relative to the shear band center. EBSD measurements were taken on both sides of the top-hat cross section (i.e., the left and right shear bands). The data from both sides of the top-hat were combined for all plots and analyses (see Supplementary Material for more details).

Nanoindentation testing was performed on an MTS Nano-XP and Keysight G200 nanoindenter using two diamond tips: a cono-spherical tip with a nominal radius of 8 μm (referred to as a 10-μm tip) and a Berkovich tip. The continuous stiffness measurement (CSM) was used at a displacement amplitude of 2 nm and frequency of 45 Hz. Spherical nanoindentation tests were run to displacements of 500–600 nm with a minimum spacing of three times the residual diameter. The measured load, P, displacement, h, and stiffness, S data were used to calculate the contact radius, a, indentation stress, $\sigma_{ind} = \frac{P}{\pi a^2}$, and strain, $\varepsilon_{ind} = \frac{4}{3\pi}\frac{h}{a}$, according to the protocols of Kalidindi and Pathak [30, 31]. Berkovich

nanoindentation tests were run to a maximum of 500 nm displacement and a minimum spacing of three times the residual indent width. Hardness was calculated using the Oliver–Pharr analysis with an area function calibrated on fused quartz [32]. Indents were made on both sides of the top-hat cross section (i.e., the left and right shear bands). The data from both sides of the top-hat were combined for all plots and analyses (see Supplementary Material for more details). Nanoindentation was chosen over microindentation because of the higher spatial resolution (ability to place many indents closely together) which can better capture the deformation gradient across the shear band. This is at the sacrifice of probing only one to two grains.

Results

Representative EBSD data

Representative EBSD image quality (IQ) maps and inverse pole figure (IPF) maps of the reduced data for wrought and AM materials are shown in Fig. 2. The reader is referred to Ref. [21] and the Supplementary Material for details on the starting microstructures prior to deformation. In Fig. 2, the shear band is defined on IQ maps by the dark regions of low IQ. The EBSD maps are rotated so that the shear band runs vertical. The shear band contains a large amount of plastic deformation and possibly very small

Figure 2 Representative EBSD data for wrought **a**, **b** and AM **c**, **d** shear band samples. Image quality maps are generated from the raw data. IPF maps are generated using the cleanup process described in the main text. Grain boundaries are displayed with black lines. White regions represent unusable data.
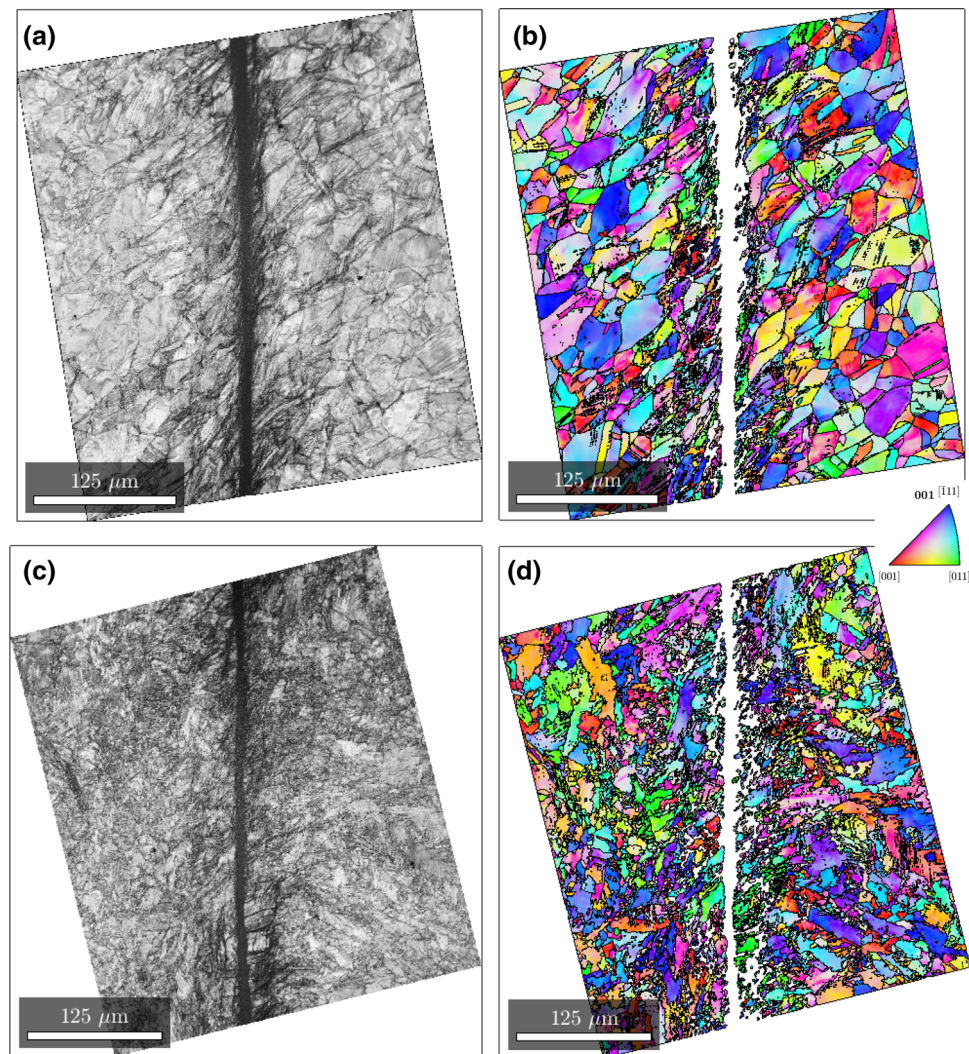
features that are not resolved with traditional EBSD. TEM on similar shear bands of wrought 316L SS shows a fine equiaxed sub-grain microstructure in the shear band core likely produced by dynamic recovery or continuous dynamic recrystallization [6]. The EBSD data were used to calculate local misorientation values as described previously. KAM and GROD are two of several commonly used local misorientation values that are used to identify areas of increased geometrically necessary dislocations and accumulated plastic strain [8–13, 18–20].

Figure 3 shows the misorientation mean, median, and mode values for KAM and GROD as a function of distance from the shear band center. After the EBSD data are rotated as in Fig. 2 so that the shear band is vertical, the data are sliced vertically into 10-µm-wide strips. The position of each strip is the perpendicular distance between the midpoint of the strip and the shear band center. In addition to the misorientation values, the percentage of useable data is also plotted in Fig. 3. Again, it becomes clear that little data remain, 5–25%, for the misorientation calculations at the shear band center which is a limitation for using EBSD to characterize the shear band center. Despite this limitation, there is a clear trend of increasing KAM and GROD approaching the shear band center. The mean misorientation values in the region just outside the shear band center are significantly above the mean misorientation values determined on undeformed samples (see Supplementary Material). For additional comparison, Bagherifard et al. [33] report maximum KAM values of 2°–2.5° on severe shot peened 316L SS which is a similar magnitude to the region just outside the shear band center in this study.
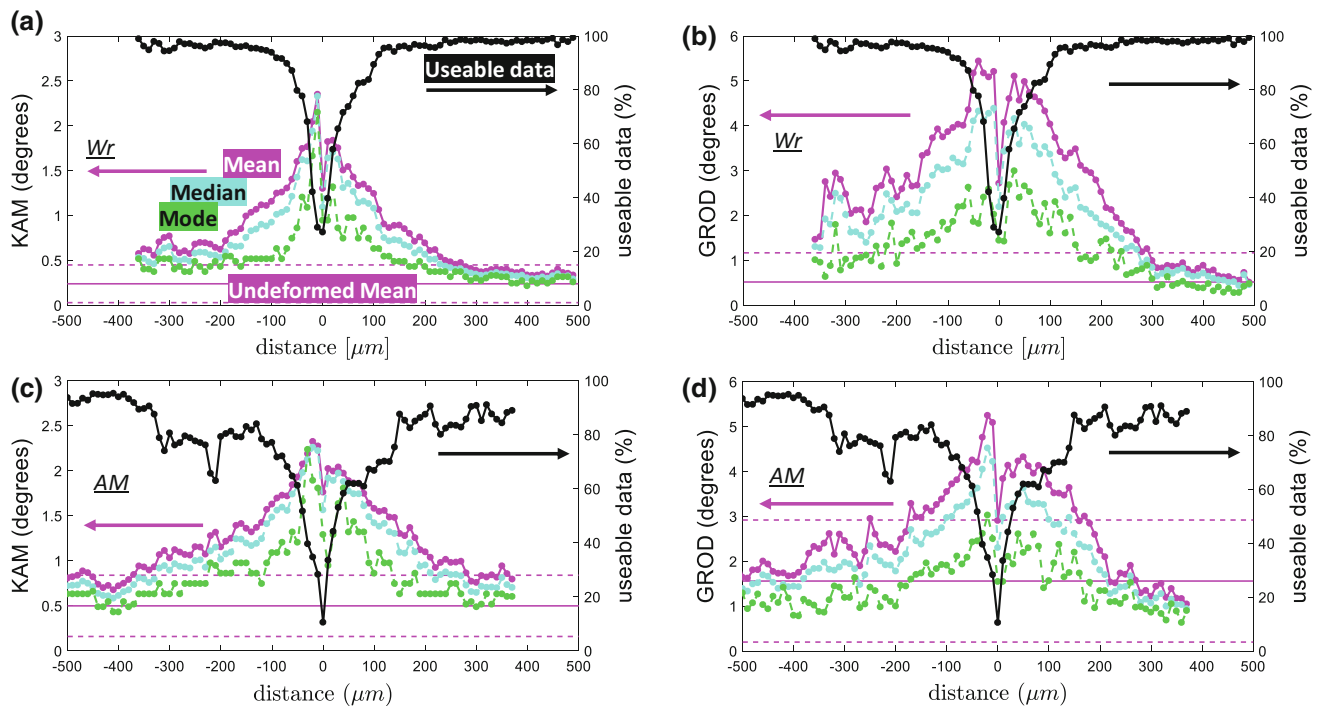
Figure 3 Mean, median, and mode KAM and GROD values for **a**, **b** wrought and **c**, **d** AM EBSD scans across shear bands. The labeling in **a** is the same for the rest of the figure unless otherwise noted. Useable data points are the percentage of pixels remaining after removing very low confidence points and very small grains. See Sect. 2 for more details. The horizontal solid and dotted lines are the mean ± 1 SD determined from undeformed samples.

Representative nanoindentation data

Nanoindentation tests with spherical and Berkovich tip geometries were performed to determine the changes in flow stress due to deformation hardening in the shear band regions. This is particularly important in stainless steels which show a significant amount of work hardening related to their resistance to form adiabatic shear bands [4]. It is important to keep in mind the volume of material probed using nanoindentation relative to microstructural features. Far from the shear band center, it is possible to completely isolate single grains; however, in the shear band center, individual grains cannot be readily isolated. Hence, to provide a better comparison across the shear band, we want the indents to probe grains and grain boundaries in all regions. Therefore, an indiscriminate approach of indent arrays across the shear band was employed. A sufficient number of indents will capture the overall trend across the shear band region without the need to account for the crystal orientation, grain boundaries, etc., at individual indentation sites.

Representative spherical indentation stress–strain curves and Berkovich hardness–displacement curves are shown in Fig. 4a, b, respectively, for deformed forced shear samples. The measurements shown occur away from the shear band (> 200 μm distance) and at the shear band center (< 50 μm distance). There are several observations in Fig. 4. First, the spherical stress–strain response shows a significant increase in indentation stress at the shear band compared to away from the shear band. The increase in indentation stress in the shear band center is likely a consequence of both an increase in dislocation density and a refinement in grain structure. Second, the indentation stress–strain response at the shear band center is very similar between the AM and wrought materials, showing that the material has hardened to a similar level despite any differences in the initial microstructure. Third, the mechanical behavior of AM material away from the shear band center shows slightly higher stresses than the wrought material; however, this difference is within the variation from site to site. More discussion of the different behavior away from the shear band center will be provided later. The representative hardness
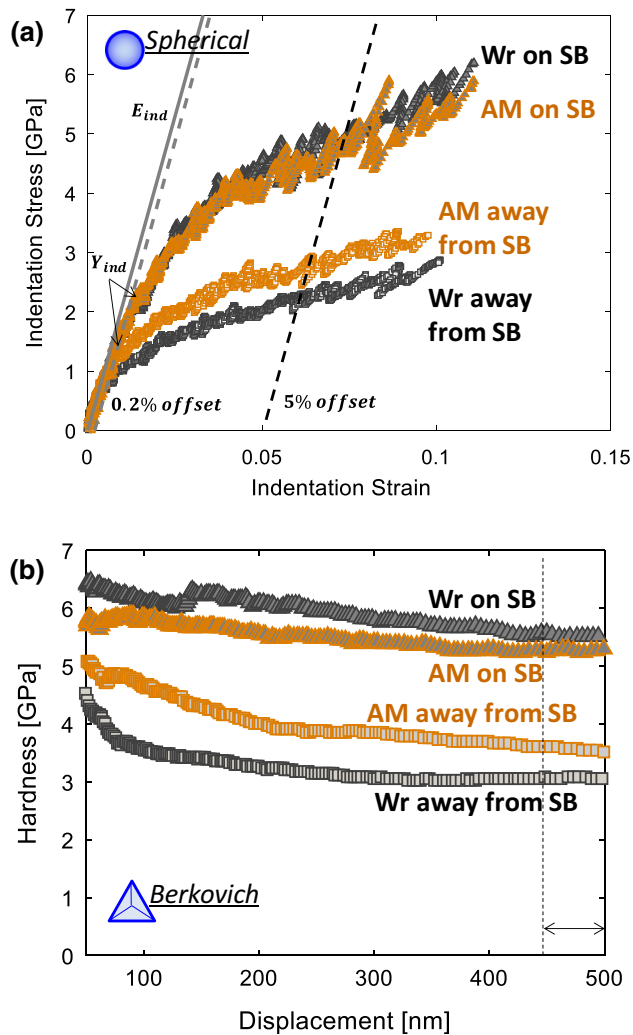
Figure 4 Representative nanoindentation data across the shear band (SB) for wrought (Wr) and AM materials. **a** 10-μm-radius SNI stress–strain curves with the indentation modulus, E_{ind}, SNI yield stress defined by a 0.2% indentation strain offset, Y_{ind}, and SNI stress at 5% indentation strain offset. **b** Berkovich nanohardness versus depth. The average hardness for each test was determined from 450 to 500 nm displacement. "Away from the shear band" is defined as > 200 μm from the SB center and "on SB" is defined as within 50 μm of the shear band center.

data in Fig. 5b are complimentary to the observations made from SNI stress–strain curves. The hardness measurements reflect a flow stress after approximately 8% average strain under the indenter [34]. Here, we point out that the hardness is beginning to reach a constant value by ≅ 500 nm displacement, and these stresses are comparable to the spherical indentation stresses after indentation strains of ≅ 10%.

The trends of SNI yield stress, SNI stress at 5% strain offset, and nanohardness are plotted against the distance from the shear band for wrought and AM materials in Fig. 5. The distance plotted on the x-axis is defined as zero at the shear band center. The positive direction is defined from the center of the specimen moving outward perpendicular to the shear band (i.e., radial direction). SNI measurements on undeformed samples are shown as horizontal solid ± dotted lines for the mean ± 1 SD (see Supplementary Material for more details). Here, we note that the SNI measurements on the undeformed wrought and AM condition do not show a 60% higher strength for AM compared to wrought that was seen in the macroscopic compression tests [21]. More discussion on this point is provided later. The SNI measurements on the wrought forced shear sample at approximately 300 μm away from the shear band center match the SNI measurements on the wrought undeformed sample. However, the AM SNI measurements on the forced shear sample remain slightly above the SNI measurements for the undeformed sample, particularly the SNI stress at 5% offset. This suggests that a wider band of material away from the shear band center has work-hardened in the AM material compared to wrought. Overall, the indentation measurements show similar trends to the EBSD misorientation trends with increasing values approaching the shear band center. A direct comparison between the wrought and AM materials is provided in the next section.

Discussion

SNI measurements of undeformed samples: wrought versus AM

As mentioned earlier, the as-built AM material showed a bulk compression yield stress ≅ 60% higher than the annealed wrought material with similar work hardening [21]. However, the spherical nanoindentation yield stress and stress at 5% strain offset are nearly identical in the undeformed annealed wrought and as-built AM materials. This is shown in Fig. 5 by the baseline measurements and with indentation stress–strain curves in Supplementary Material. The absence of an increase in flow stress measured from SNI in the AM material implies that the increase in bulk yield stress comes from
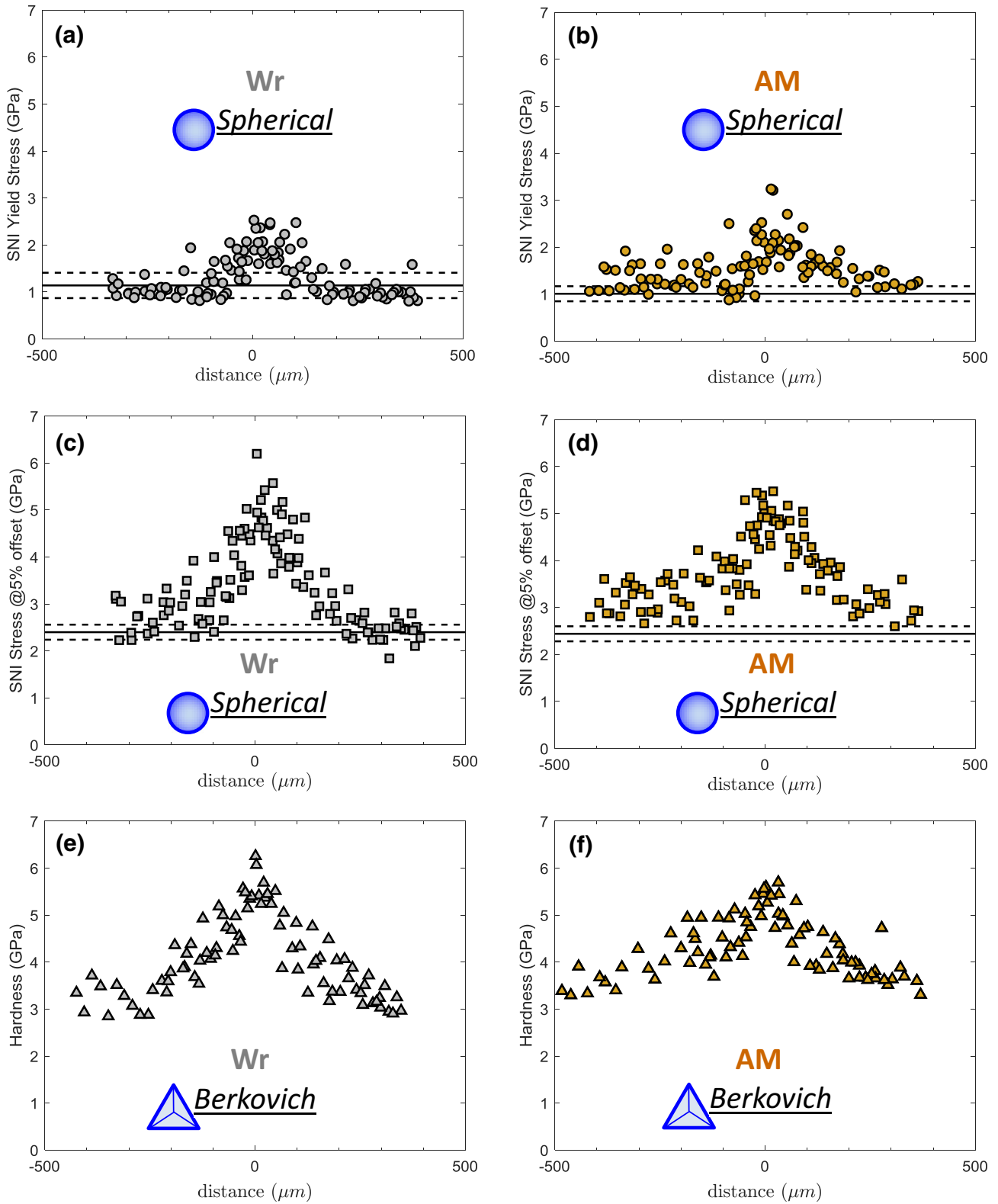
Figure 5 Nanoindentation results versus distance from the shear band center for wrought **a**, **c**, **e** and AM **b**, **d**, **f** materials. SNI yield stress and SNI stress at 5% strain offset were measured from a 10-μm-radius spherical nanoindentation tests. Hardness was measured from Berkovich nanoindentation tests. See Fig. 4 for representative data.

microstructural features or deformation processes (e.g., dislocation cell structures) that exist at a higher length scale than the material probed with SNI measurements. In other words, the grain morphology differences rather than the dislocation density differences are likely responsible for the increase in macroscopic yield stress reported for the AM material. The argument for this is as follows. The volume probed can be approximated as a cylinder with radius equal to the contact radius and height 2.4 times the contact radius [31, 35]. The average contact radius at the indentation yield stress and the final displacement with the 10-μm-radius tip is 160 ± 30 nm and 2.3 ± 0.1 μm for wrought material and 150 ± 20 nm and 2.5 ± 0.1 μm for AM material, respectively. The average grain size (equivalent diameter) is reported to be 29 μm for the wrought material and 4.5 μm with a range of 2.5–60 μm for the AM material. The indents are probing one to two grains and zero to one grain boundary depending on where the indents are placed. Therefore, the grain size and morphology differences between the wrought and AM materials should not have a significant influence on the SNI measurements. In addition to the grain size, the average dendrite spacing in the AM material is reported as 1.5–2.6 μm [21] which means the SNI measurements are probing at most a few dendritic boundaries. The dendritic structure forms due to the solidification process that occurs during AM creating chemical segregation. The dendritic boundaries are rich in Mo and Cr compared to the inter-dendritic regions [36–38]. Smith et al. [38] argue that the dendritic structure (chemical segregation of Cr) can increase the macroscopic flow stress supported by examples in directed energy deposition 304 SS. The dendritic microstructure does not appear to influence the SNI flow stress comparing the wrought and AM materials. It is possible that more dendrite boundaries need to be probed to see an effect. Changes in dislocation density should have a significant effect on the SNI flow stress as seen by the SNI trends across the heavily deformed shear bands. Bronkhorst et al. [39] estimated the dislocation densities from neutron diffraction intensity profiles using procedures outlined in Ref. [40]. The as-built AM material had a dislocation density of 2.3×10^8 mm^{-2} which is ~ 2.3 times higher than the annealed wrought material with a dislocation density of 9.0×10^7 mm^{-2}. The dislocation density in the AM material from diffraction compares well with

reported data from TEM: 2.8×10^7 mm^{-2} [23]. The 2.3 times higher dislocation density in the AM material is not significant enough to cause higher SNI flow stresses. Gray et al. [21] ruled out significant differences in dislocation density and residual stress between the annealed wrought and as-built AM materials by strain rate jump tests. However, Bronkhorst et al. [39] believe the difference in dislocation density to be the primary cause of the increase in macroscopic strength compared to grain size effects based on crystal plasticity finite element simulations. Bronkhorst et al. [39] note that the grain size effect may not be accurately captured in their model due to the uncertainty in the Hall–Petch coefficient as well as the inability of Hall–Petch-type hardening to capture grain morphology differences. It is difficult to separate out the different strengthening mechanisms as evident by the differences in the literature [21, 38, 39]. However, the SNI measurements suggest that the grain morphology differences are the primary source of increased strength rather than dislocation density or dendritic structure.

Indentation measurements of shear band samples: wrought versus AM

Figure 6 shows the direct comparison of wrought and AM material indentation trends across the shear bands. A Cauchy model regression was used to express the mean trend of the data as shown by solid lines in Fig. 6 [41]. A flat baseline was determined and subtracted prior to the regression [41]. Error bars were determined from the bootstrap method [41]. The goodness of fit in terms of r-squared, baseline, peak height, and peak position for all the regressions are given in Table 2. The regression fit lines tend to come together for the wrought and AM materials at the shear band. In addition, the total peak height, baseline + peak height, is nearly the same for both materials. This indicates that the flow stress of the material at the shear band center is identical between the wrought and AM materials. The SNI yield stress, SNI stress at 5% strain offset, and hardness away from the shear band are higher in the AM material compared to the wrought material. This difference is subtle given that the spread of individual measurements is as large as the difference; however, the difference is consistent for all three indentation measurements.
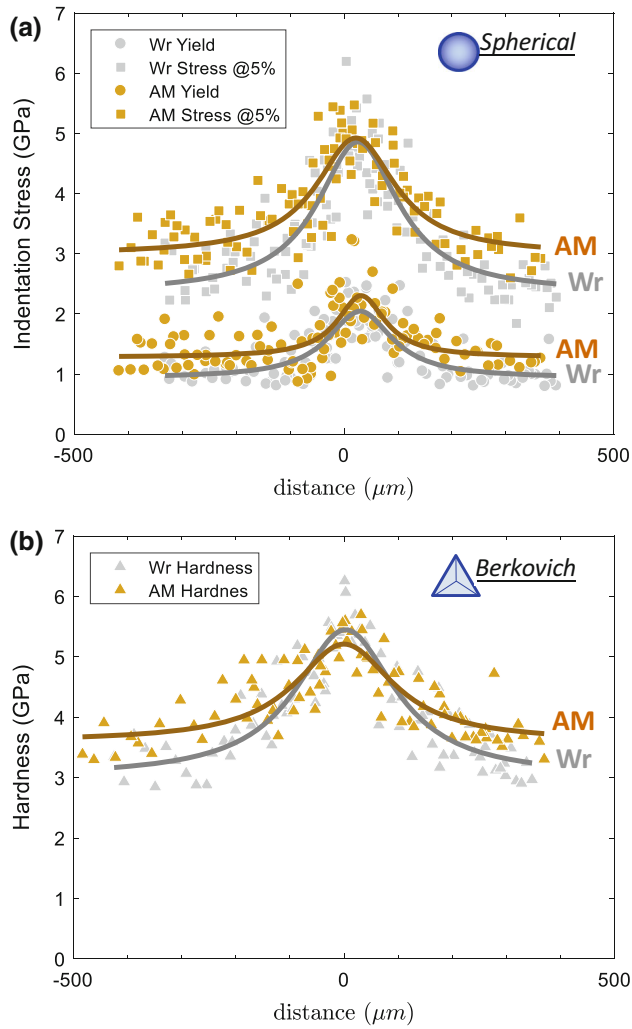
Figure 6 Cauchy model fits to nanoindentation versus distance measurements on wrought and AM shear bands: **a** SNI yield stress and SNI stress at 5% strain offset and **b** nanohardness averaged at 450–500 nm displacement. Fit parameters and uncertainties are given in Table 2.

A possible explanation for the higher indentation stress in the regions away from the shear band center requires again discussing the difference between the macroscopic response and the nanoindentation response. Recall that the AM material clearly has a higher macroscopic flow stress (Ref. [21]) while having similar SNI flow stress compared to the wrought. Based on the arguments presented in "SNI measurements of undeformed samples: wrought versus AM" section, it is believed that the grain size and morphology differences are the reason for this. The forced shear band test is a macroscopically applied deformation such that these differences will play a role in the deformation process. Here, we assume that the smaller grain size and as-built grain morphology lead to the accumulation of higher dislocation densities in the as-built material around the shear band. This causes higher indentation stresses. Eventually, the dislocation densities and work hardening saturate, and the difference between the AM and wrought materials disappears in the very center of the shear band. A better understanding of how the deformation evolves during earlier stages of the deformation can come from interrupted forced shear tests with corresponding indentation measurements.

Comparison of EBSD misorientation and spherical nanoindentation data

Another interesting result from these experiments was that the EBSD misorientation and nanoindentation measurements showed very similar trends across the shear band in the wrought and AM materials. As mentioned previously, there are few studies that directly correlate EBSD misorientation

Table 2 Cauchy model fit results for nanoindentation versus distance measurements

Variable	R^2	Baseline (GPa)	Peak height (GPa)	Peak position (μm)	Peak width (μm)
Wr SNI yield	0.609	0.93	1.12 ± 0.07	31 ± 5	152 ± 20
AM SNI yield	0.460	1.28	1.03 ± 0.12	32 ± 7	108 ± 24
Wr SNI stress@5%	0.751	2.35	2.54 ± 0.10	26 ± 4	184 ± 17
AM SNI stress@5%	0.712	2.99	1.95 ± 0.08	22 ± 5	179 ± 16
Wr hardness	0.801	3.01	2.45 ± 0.10	3 ± 4	229 ± 27
AM hardness	0.674	3.59	1.66 ± 0.11	-1 ± 8	232 ± 68

Error measurements are ± 1 SD generated using a Bootstrap method. The goodness of fit is given in terms of r-squared, R^2. A flat baseline correction and a single peak were used for the model fit. The peak height is the difference between the baseline and absolute peak height. See Ref. [41] for more details of the regression analysis

and nanoindentation after macroscopic deformation (e.g., [18, 19]). EBSD misorientation and nanoindentation measurements can be related through the relationship between dislocation density and flow stress using the Taylor hardening law, Taylor factor, and constraint factor between indentation and uniaxial yield strength:

$$\tau = \alpha \mu b \sqrt{\rho}, \tag{1}$$

$$\sigma_{ys} = M\tau, \tag{2}$$

$$Y_{ind} \approx 2\sigma_{ys}, \tag{3}$$

where τ is the shear flow stress, α is the barrier strength coefficient, μ is the shear modulus, b is the Burger's vector, and ρ is the total dislocation density. The shear flow stress is related to the uniaxial yield strength, σ_{ys}, by the Taylor factor, M, which is 3.067 on average. Here, we have chosen to focus on the SNI yield stress, which is a measure of the initial flow stress during indentation rather than after significant plastic deformation under the indenter. For an isotropic material that follows J2 flow theory, the constraint factor is $\cong 2$ [42]. Local misorientation values represent the geometrically necessary dislocations, ρ_{GND}, which is a portion of the total dislocation density. The simplest estimate of the GND density from strain gradient plasticity theory is

$$\rho_{GND} = \frac{2\theta}{Lb}, \tag{4}$$

where the GND density depends on the misorientation angle, θ, the step size, L, and the Burger's vector, b [43, 44]. Combining all these equations using $\alpha = 0.3$ [44], $b = 0.255$ from a calculated lattice parameter of 0.361 nm using Ref. [45] and $L = 0.6$ μm give an estimate of the indentation yield stress from the misorientation measurements:

$$Y_{ind} \cong (2)(3.067)\alpha\mu b \sqrt{\frac{2\theta}{Lb}} = 4.292\sqrt{\theta}. \tag{5}$$

Note that the above equation estimates the SNI yield stress solely based on the GNDs and does not include the contribution of the statistically stored dislocations. Therefore, it is expected to underpredict the flow stress and subsequent indentation yield stress.

Figure 7 shows the predicted SNI yield stress based on the average KAM and GROD values using Eq. (5) compared with the measured SNI yield stress. Both are plotted versus the distance from the shear band. The earlier observation of KAM and GROD measurements showing similar trends to nanoindentation measurements is still visible in Fig. 7. However, the predicted SNI yield stress from KAM measurements significantly underestimates the actual SNI yield stress across the entire shear band. This is partly due to the SSDs unaccounted for in the prediction. There is also a degree of uncertainty in the barrier strength coefficient and constraint factor. The SNI yield stress predictions from GROD measurements are in better agreement than those from KAM measurements; however, it is not conventional to use GROD values for GND calculations. The GND calculation is based on a local crystal lattice curvature. GROD is not local in this sense because it considers information from an entire grain. Furthermore, the value of L in Eq. (5) does not have the same physical meaning when using KAM versus GROD. For KAM, this term describes the distance over which the misorientation angle was calculated. Since GROD values are based on the average grain orientation, it is not clear how to define L, but it is likely larger than the value of 600 nm step size and closer to the grain size. Increasing L would lower the predicted SNI yield stress. For both KAM and GROD, the pronounced peak on the shear band center is missing in the predicted SNI yield stress. This is due to a lack of useable data in the heavily deformed shear band due to very high dislocation densities and/or smaller features than the interaction volume that degrade the pattern quality. Advanced EBSD techniques such as TKD [46] and dictionary methods [47, 48] might be able to recover more information in the shear band center. Indentation testing is able to provide information in this region, which shows that the flow stress is significantly higher than away from the shear band. The indentation response is also affected by the total dislocation density and not just the GND density. In theory, the SNI yield stress measurement does not further work-harden the material under the indenter compared to the measurements of hardness or SNI stress at 5% strain offset. However, the SNI yield stress may be more sensitive to tip and surface asperities and analyses protocols. In this study, all three indentation measurements presented show similar trends.
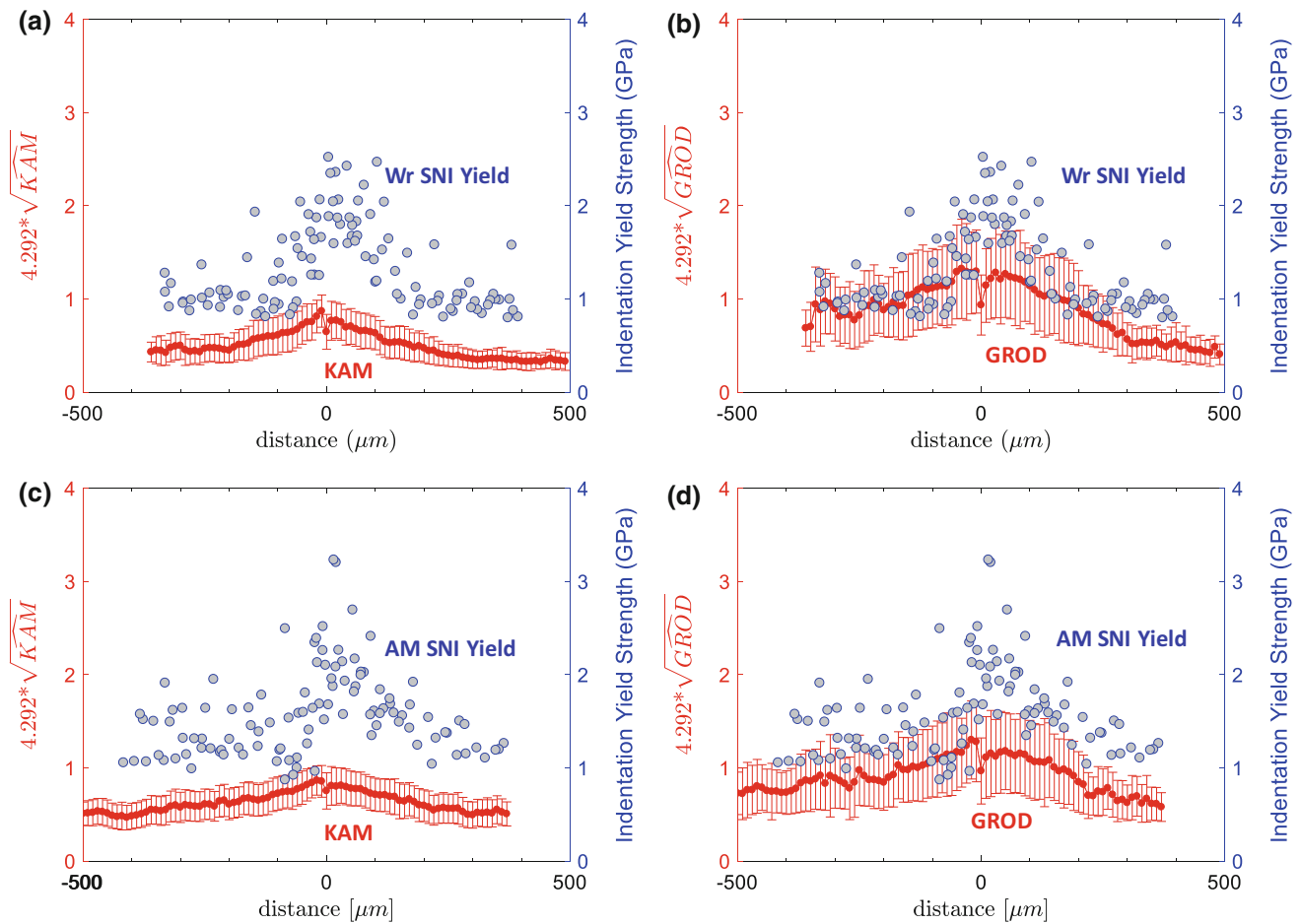
Figure 7 Comparison of spherical nanoindentation (SNI) yield stress with KAM and GROD misorientation values for **a**, **b** wrought (Wr) and **c**, **d** additively manufactured (AM) materials. Error bars were propagated using ± SD for the *y*-axis calculation.

Conclusions

The mechanical response of annealed wrought and directed energy deposition additively manufactured 316L SS were compared using a macroscopic forced shear test followed by EBSD and nanoindentation characterization of the shear band region. The findings are:

1. Despite significant differences in the microstructure, quasi-static mechanical properties, and dynamic properties between the wrought and AM materials, the maximum nanoindentation stresses occur in the shear band center with similar magnitudes. The indentation stresses in the undeformed condition are similar, and only minor differences exist in the indentation stress profiles away from the shear band center with slightly higher values for the AM material. Interrupted force shear tests at different total

displacements are needed to understand differences in how the shear band evolves between the wrought and AM materials. The SNI yield stress, SNI stress at 5% strain offset, and hardness measurements across the shear band can be used to inform adiabatic shear band models, particularly the amount of work hardening that occurs as a function of the distance from the shear band center.

2. Nanoindentation and EBSD misorientation measurements provide complementary information about the increase in dislocation density across the shear band as a result of the macroscopically applied force shear test. KAM and GROD local misorientation measurements were directly compared to the SNI yield stress through the calculation of GNDs and conversion from uniaxial to indentation stress. Predictions from KAM values underestimate the SNI yield stress due to the fact

that the GNDs are only a portion of the overall dislocation population. Predictions from GROD values provide better agreement since they have higher magnitudes than KAM. Neither misorientation measurement can predict the SNI yield stress nor work hardening occurs in the shear band center due to the lack of useable EBSD data from this region. The combination of nanoindentation and EBSD provides a rich amount of information about the local changes in dislocation density due to macroscopically applied deformation. The data suggest that there is a strong relationship between both measurements.

Acknowledgements

Compliance with ethical standards

Conflict of interest   The authors declare that they have no conflict of interests.

Electronic supplementary material: The online version of this article (https://doi.org/10.1007/s10853-019-03994-8) contains supplementary material, which is available to authorized users.

References

[1] Kok Y, Tan XP, Wang P, Nai MLS, Loh NH, Liu E, Tor SB (2018) Anisotropy and heterogeneity of microstructure and mechanical properties in metal additive manufacturing: a critical review. Mater Des 139:565–586. https://doi.org/10.1016/j.matdes.2017.11.021

[2] Fayazfar H, Salarian M, Rogalsky A, Sarker D, Russo P, Paserin V, Toyserkani E (2018) A critical review of powder-based additive manufacturing of ferrous alloys: process parameters, microstructure and mechanical properties. Mater Des 144:98–128. https://doi.org/10.1016/j.matdes.2018.02.018

[3] DebRoy T, Wei HL, Zuback JS, Mukherjee T, Elmer JW, Milewski JO, Beese AM, Wilson-Heid A, De A, Zhang W (2018) Additive manufacturing of metallic components—process, structure and properties. Prog Mater Sci 92:112–224. https://doi.org/10.1016/j.pmatsci.2017.10.001

[4] Xue Q, Gray GT (2006) Development of adiabatic shear bands in annealed 316L stainless steel: part I. Correlation between evolving microstructure and mechanical behavior. Metall Mater Trans A 37(8):2435–2446

[5] Dodd B (1992) Adiabatic shear localization: occurrence, theories, and applications. Pergamon Press, Oxford

[6] Xue Q, Gray G (2006) Development of adiabatic shear bands in annealed 316L stainless steel: part II. TEM studies of the evolution of microstructure during deformation localization. Metall Mater Trans A 37(8):2447–2458

[7] Xue Q, Cerreta EK, Gray GT (2007) Microstructural characteristics of post-shear localization in cold-rolled 316L stainless steel. Acta Mater 55(2):691–704. https://doi.org/10.1016/j.actamat.2006.09.001

[8] Wright SI, Nowell MM, Field DP (2011) A review of strain analysis using electron backscatter diffraction. Microsc Microanal 17(3):316–329

[9] Pantleon W (2008) Resolving the geometrically necessary dislocation content by conventional electron backscattering diffraction. Scr Mater 58(11):994–997

[10] Ruggles TJ, Fullwood DT (2013) Estimations of bulk geometrically necessary dislocation density using high resolution EBSD. Ultramicroscopy 133:8–15. https://doi.org/10.1016/j.ultramic.2013.04.011

[11] Wilkinson AJ, Meaden G, Dingley DJ (2006) High resolution mapping of strains and rotations using electron backscatter diffraction. Mater Sci Technol 22(11):1271–1278

[12] Zhu C, Harrington T, Livescu V, Gray GT, Vecchio KS (2016) Determination of geometrically necessary dislocations in large shear strain localization in aluminum. Acta Mater 118:383–394. https://doi.org/10.1016/j.actamat.2016.07.051

[13] Shen RR, Efsing P (2018) Overcoming the drawbacks of plastic strain estimation based on KAM. Ultramicroscopy 184:156–163. https://doi.org/10.1016/j.ultramic.2017.08.013

[14] Zhu C, Livescu V, Harrington T, Dippo O, Gray GT, Vecchio KS (2017) Investigation of the shear response and geometrically necessary dislocation densities in shear localization in high-purity titanium. Int J Plast 92:148–163. https://doi.org/10.1016/j.ijplas.2017.03.009

[15] Pathak S, Stojakovic D, Kalidindi SR (2009) Measurement of the local mechanical properties in polycrystalline samples using spherical nanoindentation and orientation imaging

microscopy. Acta Mater 57(10):3020–3028. https://doi.org/10.1016/j.actamat.2009.03.008

[16] Vachhani SJ, Kalidindi SR (2015) Grain-scale measurement of slip resistances in aluminum polycrystals using spherical nanoindentation. Acta Mater 90:27–36. https://doi.org/10.1016/j.actamat.2015.02.017

[17] Weaver JS, Jones DR, Li N, Mara N, Fensin S, Gray GT III (2018) Quantifying heterogeneous deformation in grain boundary regions on shock loaded tantalum using spherical and sharp tip nanoindentation. Mater Sci Eng A 737:373–382

[18] Dziaszyk S, Payton EJ, Friedel F, Marx V, Eggeler G (2010) On the characterization of recrystallized fraction using electron backscatter diffraction: a direct comparison to local hardness in an IF steel using nanoindentation. Mater Sci Eng A 527(29):7854–7864. https://doi.org/10.1016/j.msea.2010.08.063

[19] Shen RR, Ström V, Efsing P (2016) Spatial correlation between local misorientations and nanoindentation hardness in nickel–base alloy 690. Mater Sci Eng A 674:171–177. https://doi.org/10.1016/j.msea.2016.07.123

[20] Guglielmi PO, Ziehmer M, Lilleodden ET (2018) On a novel strain indicator based on uncorrelated misorientation angles for correlating dislocation density to local strength. Acta Mater 150:195–205. https://doi.org/10.1016/j.actamat.2018.03.009

[21] Gray GT, Livescu V, Rigg PA, Trujillo CP, Cady CM, Chen SR, Carpenter JS, Lienert TJ, Fensin SJ (2017) Structure/property (constitutive and spallation response) of additively manufactured 316L stainless steel. Acta Mater 138:140–149. https://doi.org/10.1016/j.actamat.2017.07.045

[22] Griffith M, Schlienger M, Harwell L, Oliver M, Baldwin M, Ensz M, Essien M, Brooks J, Robino C, Smugeresky EJ (1999) Understanding thermal behavior in the LENS process. Mater Des 20(2–3):107–113

[23] Morrow BM, Lienert TJ, Knapp CM, Sutton JO, Brand MJ, Pacheco RM, Livescu V, Carpenter JS, Gray GT (2018) Impact of defects in powder feedstock Materials on Microstructure of 304L and 316L stainless steel produced by additive manufacturing. Metall Mater Trans A 49(8):3637–3650. https://doi.org/10.1007/s11661-018-4661-9

[24] Yadollahi A, Shamsaei N, Thompson SM, Seely DW (2015) Effects of process time interval and heat treatment on the mechanical and microstructural properties of direct laser deposited 316L stainless steel. Mater Sci Eng A 644:171–183. https://doi.org/10.1016/j.msea.2015.07.056

[25] Wang Z, Palmer TA, Beese AM (2016) Effect of processing parameters on microstructure and tensile properties of austenitic stainless steel 304L made by directed energy deposition additive manufacturing. Acta Mater 110:226–235. https://doi.org/10.1016/j.actamat.2016.03.019

[26] Gray GT, Vecchio KS, Livescu V (2016) Compact forced simple-shear sample for studying shear localization in materials. Acta Mater 103:12–22. https://doi.org/10.1016/j.actamat.2015.09.051

[27] Bronkhorst CA, Cerreta EK, Xue Q, Maudlin PJ, Mason TA, Gray GT (2006) An experimental and numerical study of the localization behavior of tantalum and stainless steel. Int J Plast 22(7):1304–1335. https://doi.org/10.1016/j.ijplas.2005.10.002

[28] Xue Q, Gray GT, Henrie BL, Maloy SA, Chen SR (2005) Influence of shock prestraining on the formation of shear localization in 304 stainless steel. Metall Mater Trans A 36(6):1471–1486. https://doi.org/10.1007/s11661-005-0239-4

[29] Bachmann F, Hielscher R, Schaeben H (2010) Texture analysis with MTEX—free and open source software toolbox. In: Klein H, Schwarzer RA (eds) Solid state phenomena. Trans Tech Publication, Zurich, pp 63–68

[30] Pathak S, Kalidindi SR (2015) Spherical nanoindentation stress–strain curves. Mater Sci Eng R 91:1–36. https://doi.org/10.1016/j.mser.2015.02.001

[31] Kalidindi SR, Pathak S (2008) Determination of the effective zero-point and the extraction of spherical nanoindentation stress–strain curves. Acta Mater 56(14):3523–3532. https://doi.org/10.1016/j.actamat.2008.03.036

[32] Oliver WC, Pharr GM (2004) Measurement of hardness and elastic modulus by instrumented indentation: advances in understanding and refinements to methodology. J Mater Res 19(1):3–20. https://doi.org/10.1557/jmr.2004.19.1.3

[33] Bagherifard S, Slawik S, Fernández-Pariente I, Pauly C, Mücklich F, Guagliano M (2016) Nanoscale surface modification of AISI 316L stainless steel by severe shot peening. Mater Des 102:68–77

[34] Tabor D (1956) The physical meaning of indentation and scratch hardness. Br J Appl Phys 7(5):159–166

[35] Donohue BR, Ambrus A, Kalidindi SR (2012) Critical evaluation of the indentation data analyses methods for the extraction of isotropic uniaxial mechanical properties using finite element models. Acta Mater 60(9):3943–3952. https://doi.org/10.1016/j.actamat.2012.03.034

[36] Wang YM, Voisin T, McKeown JT, Ye J, Calta NP, Li Z, Zeng Z, Zhang Y, Chen W, Roehling TT, Ott RT, Santala MK, Depond Philip J, Matthews MJ, Hamza AV, Zhu T (2017) Additively manufactured hierarchical stainless steels with high strength and ductility. Nat Mater 17:63–71. https://doi.org/10.1038/nmat5021

[37] Gorsse S, Hutchinson C, Gouné M, Banerjee R (2017) Additive manufacturing of metals: a brief review of the

characteristic microstructures and properties of steels, Ti–6Al–4V and high-entropy alloys. Sci Technol Adv Mater 18(1):584–610. https://doi.org/10.1080/14686996.2017.1361305

[38] Smith TR, Sugar JD, San Marchi C, Schoenung JM (2019) Strengthening mechanisms in directed energy deposited austenitic stainless steel. Acta Mater 164:728–740. https://doi.org/10.1016/j.actamat.2018.11.021

[39] Bronkhorst CA, Mayeur JR, Livescu V, Pokharel R, Brown DW, Gray GT (2019) Structural representation of additively manufactured 316L austenitic stainless steel. Int J Plast 118:70–86. https://doi.org/10.1016/j.ijplas.2019.01.012

[40] Brown D, Adams D, Balogh L, Carpenter J, Clausen B, King G, Reedlunn B, Palmer T, Maguire M, Vogel S (2017) In situ neutron diffraction study of the influence of microstructure on the mechanical response of additively manufactured 304L stainless steel. Metall Mater Trans A 48(12):6055–6069

[41] O'Haver T (1997) A pragmatic introduction to signal processing. https://terpconnect.umd.edu/~toh/spectrum/TOC.html. Accessed 9 Sept 2019

[42] Patel DK, Kalidindi SR (2016) Correlation of spherical nanoindentation stress–strain curves to simple compression stress–train curves for elastic–plastic isotropic materials using finite element models. Acta Mater 112:295–302. https://doi.org/10.1016/j.actamat.2016.04.034

[43] Gao H, Huang Y, Nix WD, Hutchinson JW (1999) Mechanism-based strain gradient plasticity—I. Theory. J Mech Phys Solids 47(6):1239–1263. https://doi.org/10.1016/S0022-5096(98)00103-3

[44] Kubin L, Mortensen A (2003) Geometrically necessary dislocations and strain-gradient plasticity: a few critical issues. Scr Mater 48(2):119–125

[45] Lee S-J, Lee Y-K (2005) Quantitative analyses of ferrite lattice parameter and solute Nb content in low carbon microalloyed steels. Scr Mater 52(10):973–976

[46] Trimby PW (2012) Orientation mapping of nanostructured materials using transmission Kikuchi diffraction in the scanning electron microscope. Ultramicroscopy 120:16–24. https://doi.org/10.1016/j.ultramic.2012.06.004

[47] Chen YH, Park SU, Wei D, Newstadt G, Jackson MA, Simmons JP, De Graef M, Hero AO (2015) A dictionary approach to electron backscatter diffraction indexing. Microsc Microanal 21(3):739–752

[48] Singh S, Guo Y, Winiarski B, Burnett TL, Withers PJ, De Graef M (2018) High resolution low kV EBSD of heavily deformed and nanocrystalline Aluminium by dictionary-based indexing. Sci Rep 8:10991. https://doi.org/10.1038/s41598-018-29315-8